The Astrophysical Journal Letters, 931:L31 (9pp), 2022 June 1 https://doi.org/10.3847/2041-8213/ac69ca

Discovery of a 500 au Protobinary in the Massive Prestellar Core G11.92–0.61 MM2

C. J. Cyganowski[1], J. D. Ilee[2], C. L. Brogan[3], T. R. Hunter[3,4], S. Zhang (张遂楠)[1], T. J. Harries[5], and T. J. Haworth[6]
[1] Scottish Universities Physics Alliance (SUPA), School of Physics and Astronomy, University of St. Andrews, North Haugh, St. Andrews KY16 9SS, UK
cc243@st-andrews.ac.uk
[2] School of Physics and Astronomy, University of Leeds, Leeds LS2 9JT, UK
[3] National Radio Astronomy Observatory, 520 Edgemont Road, Charlottesville, VA 22903, USA
[4] Center for Astrophysics | Harvard & Smithsonian, Cambridge, MA 02138, USA
[5] Department of Physics and Astronomy, University of Exeter, Stocker Road, Exeter EX4 4QL, UK
[6] Astronomy Unit, School of Physics and Astronomy, Queen Mary University of London, London E1 4NS, UK
Received 2022 March 28; revised 2022 April 12; accepted 2022 April 23; published 2022 June 1

Abstract

We present high-resolution ($\lesssim$160 au) Atacama Large Millimeter/submillimeter Array (ALMA) 1.3 mm observations of the high-mass prestellar core candidate G11.92−0.61 MM2, which reveal that this source is in fact a protobinary system with a projected separation of 505 au. The binary components, MM2E and MM2W, are compact (radii <140 au) sources within the partially optically thick dust emission with $\alpha_{0.9\ \mathrm{cm}-1.3\ \mathrm{mm}} = 2.47$–$2.94$. The 1.3 mm brightness temperatures, $T_b = 68.4/64.6$ K for MM2E/MM2W, imply internal heating and minimum luminosities $L_* > 24.7\,L_\odot$ for MM2E and $L_* > 12.6\,L_\odot$ for MM2W. The compact sources are connected by a "bridge" of lower-surface-brightness dust emission and lie within more extended emission that may correspond to a circumbinary disk. The circumprotostellar gas mass, estimated from ∼0.″2 resolution VLA 0.9 cm observations assuming optically thin emission, is $6.8 \pm 0.9\ M_\odot$. No line emission is detected toward MM2E and MM2W in our high-resolution 1.3 mm ALMA observations. The only line detected is ^{13}CO $J = 2$–1, in absorption against the 1.3 mm continuum, which likely traces a layer of cooler molecular material surrounding the protostars. We also report the discovery of a highly asymmetric bipolar molecular outflow that appears to be driven by MM2E and/or MM2W in new deep, ∼0.″5 resolution (1685 au) ALMA 0.82 mm observations. This outflow, traced by low-excitation CH_3OH emission, indicates ongoing accretion onto the protobinary system. Overall, the super-Alfvénic models of Mignon-Risse et al. agree well with the observed properties of the MM2E/MM2W protobinary, suggesting that this system may be forming in an environment with a weak magnetic field.

Unified Astronomy Thesaurus concepts: Star formation (1569); Star forming regions (1565); Protostars (1302); Stellar accretion (1578); Binary stars (154); Stellar accretion disks (1579)

1. Introduction

Binarity and multiplicity are conspicuous characteristics of main-sequence O- and early-B-type stars (e.g., Chini et al. 2012; Sana et al. 2014; Gravity Collaboration et al. 2018) that must be explained by models of high-mass star formation. While recent observational advances have revealed binaries in massive young stellar objects (MYSOs; e.g., Beltrán et al. 2016; Beuther et al. 2017; Kraus et al. 2017; Pomohaci et al. 2019; Zapata et al. 2019; Zhang et al. 2019; Tanaka et al. 2020; Koumpia et al. 2021), all of these sources are already infrared bright and/or evolved enough for the binary components to excite hypercompact (HC) or ultracompact (UC) H II regions. There thus remains a lack of observational evidence for the earliest stages of high-mass binary formation.

These early stages, however, are important for constraining models of high-mass star formation, which differ in their predictions for the formation pathways and mass ratios of young binary or multiple systems. Modeling the collapse of isolated massive prestellar cores including turbulence and radiative and outflow feedback, Rosen & Krumholz (2020) find that companion stars form via turbulent fragmentation at early times and via disk fragmentation at late times (while with a strong magnetic field, no companion stars are formed). Other recent magnetohydronamic (e.g., Mignon-Risse et al. 2021) and hydrodynamic (e.g., Oliva & Kuiper 2020) models of the collapse of massive cores indicate that binaries form via disk rather than core fragmentation, with disk spiral arms playing an important role. While the binary formed in the early radiation-hydrodynamic simulations of Krumholz et al. (2009) consists of two high-mass stars, many subsequent works (e.g., Rosen et al. 2016; Meyer et al. 2018; Rosen et al. 2019; Rosen & Krumholz 2020) instead predict the formation of hierarchical systems with a single high-mass member. Notable recent exceptions are the super-Alfvénic cases of Mignon-Risse et al. (2021), which form stable binary systems with mass ratios of ≈1.1–1.6 and separations of a few hundred astronomical units.

Observationally, massive prestellar cores such as those adopted as initial conditions in the aforementioned simulations have proven elusive (e.g., Redaelli et al. 2021 and references therein). Among the longest-standing candidates is G11.92−0.61 MM2 (hereafter MM2): the second-brightest millimeter continuum core in the G11.92−0.61 protocluster (Cyganowski et al. 2011, 2017). MM2 was identified as a candidate massive prestellar core based on its lack of molecular line emission and other star formation indicators in Submillimeter Array (SMA) and Karl G. Jansky Very Large Array (VLA) observations (Cyganowski et al. 2014). MM2 is only ∼7.″2 (0.12 pc) from G11.92−0.61-MM1, a proto-O star with a fragmented Keplerian disk (Ilee et al. 2016, 2018); as in Cyganowski et al. (2014, 2017), here we adopt

$d_{\rm MM2} = 3.37^{+0.39}_{-0.32}$ kpc, the maser parallax distance for MM1 (Sato et al. 2014). From the SMA dust continuum, Cyganowski et al. (2014) estimated that MM2's mass is $M \gtrsim 30\ M_\odot$ within a radius $<$1000 au.

In this Letter, we present the serendipitous discovery that MM2 is a candidate (proto)binary in new high-resolution ($\lesssim$0.″05, $\lesssim$160 au) 1.3 mm Atacama Large Millimeter/Submillimeter Array (ALMA) observations targeting the MM1 disk. To better understand the properties and evolutionary states of the binary components, we complement these data with VLA 3 and 0.9 cm continuum observations (resolution $\sim$0.″2 $\sim$ 700 au) and lower-resolution ($\sim$0.″5 $\sim$ 1700 au) ALMA 0.82 and 1.05 mm observations.

2. Observations

Here we describe the new ALMA data presented in this Letter; for completeness, Table 1 summarizes observational parameters for all data sets used in our analysis. Estimated absolute flux calibration uncertainties are 5% for the ALMA and VLA 3 cm data and 10% for the VLA 0.9 cm data. All measurements were made from images corrected for the primary beam response.

Our Cycle 6 1.3 mm ALMA observations (PI: Ilee) were calibrated using the ALMA science pipeline (CASA 5.6.1-6). The approach described in Brogan et al. (2016), Cyganowski et al. (2017) was used to identify line-free channels and construct a pseudo-continuum data set; the resulting aggregate continuum bandwidth is $\sim$0.72 GHz. The continuum data were iteratively self-calibrated and the solutions applied to the line data. We combined these new C43-8 data with the C40-7 data from Ilee et al. (2018) taken with a nearly identical tuning. Combined continuum images were made using multifrequency synthesis, two Taylor terms (to account for the spectral index of the emission across the observed bandwidth), multiscale clean, and Briggs weighting with a range of values of the robust (R) parameter (see Table 1). The combined line data were imaged with $R = 0.5$ and a common velocity resolution of 0.7 km s^{-1}. We estimate the absolute positional uncertainty of the combined images as 7.4 mas. As the 1.3 mm ALMA pointings were centered on MM1, MM2 lies at the $\sim$83% level of the primary beam in these data.

Our 0.82 mm ALMA data (PI: Cyganowski) were calibrated using the ALMA science pipeline (CASA 5.4.0). We similarly constructed a pseudo-continuum data set (aggregate continuum bandwidth $\sim$0.44 GHz), iteratively self-calibrated the continuum, and applied the solutions to the line data. Here we consider only the CH_3OH $4_{-1,3}$–$3_{0,3}$ line within the wide spectral window (spw) included in the tuning to provide continuum sensitivity; results for the targeted N_2H^+(4–3) line will be presented in a forthcoming publication (S. Zhang et al. 2022, in preparation). The CH_3OH $4_{-1,3}$–$3_{0,3}$ line was imaged with a velocity resolution of 1.0 km s^{-1}.

3. Results

3.1. ALMA 1.3 mm Continuum Emission

Figure 1 shows our ALMA 1.3 mm continuum images of G11.92−0.61 MM2. The most striking feature of these high-resolution images (beam $\lesssim$160 au; Figures 1(b) and (c)) is that the 1.3 mm continuum is clearly resolved into two compact sources, which we designate MM2E and MM2W. These two compact sources are connected by a "bridge" of lower-surface-brightness emission; diffuse, low-surface-brightness emission also extends N/NW of MM2W (labeled "Diffuse" in Figure 1(c)) and to the south of the connecting bridge.

To characterize the properties of the compact sources, we fit the $R = -1.0$ 1.3 mm continuum image with two-dimensional Gaussians. Three components are required to represent the emission: one each for MM2E and MM2W and a third, more extended component for the diffuse emission. The fitted properties of these components are given in Table 2, and the fitting results are illustrated in Figures 1(d)–(f). Notably, the residual image contains an $\sim 8.1\sigma$ peak coincident with MM2E (0.″017 $\sim$ 57 au N/NW of its fitted position), indicating that this source is not entirely Gaussian. There is also an $\sim 8.5\sigma$ peak 0.″083 ($\sim$280 au) S/SW of MM2E. Both residuals suggest the existence of further substructure, including possible further multiplicity unresolved by our observations.

The projected separation between MM2E and MM2W is 0.″1499 $\sim$ 505 au. Their connecting "bridge," detected with $10\sigma < {\rm S/N} < 11\sigma$ in the compact-component-only image (Figure 1(d)), has a width of $\sim$0.″03 $\sim$ 100 au, estimated from the 10σ contour. The compact sources lie within larger structure(s), as shown by the differences in the $R = 1$, 0, and -1 images (Figures 1(a)–(c)) and the need for a diffuse component in fitting the $R = -1$ image. Using CASA's IMSTAT task, we estimate the integrated flux density (S_ν) of $>4\sigma$ emission as $\approx$107($\pm$6), 77($\pm$3), and 58($\pm$5) mJy for the $R = 1$, 0, and -1 images, respectively (uncertainties estimated following Cyganowski et al. 2012). As expected, more extended emission is also detected in the lower-resolution images: the $R = 1$ image recovers filamentary emission extending $\sim$1.″5 (5000 au) N/NW of MM2W (beyond the field of Figure 1; see also Section 3.4), and the E–W extent of $>4\sigma$ emission around MM2E/MM2W is $\sim$1.″2, 0.″8, and 0.″4 in the $R = 1$, 0, and -1 images. Even in the $R = -1$ image, the diffuse component accounts for 58% ± 4% of the fitted integrated flux density (Table 2).

3.2. Spectral Index and VLA cm Continuum Emission

To constrain the spectral indices (α) of MM2E and MM2W, we combine our new ALMA 1.3 mm images with previously published 0.9 cm and 3 cm VLA data (Table 1). To achieve the best compromise between angular resolution and sensitivity, we reimaged the 0.9 cm data with $R = 0$ (using two Taylor terms and multifrequency synthesis, as described in Ilee et al. 2016). The emission is elongated E–W (Figure 1(g); see also Hunter et al. 2015) with a morphology consistent with two sources only marginally resolved. Notably, at 0.9 cm the eastern source is brighter, while at 1.3 mm the western source is brighter (Figures 1(a)–(c), and (h)), although the latter includes contributions from MM2W and the diffuse component discussed in Section 3.1. To visualize the variation in spectral index across MM2, Figure 1(i) shows the $\alpha_{\rm 0.9\ cm-1.3\ mm}$ image calculated from the images in Figures 1(g) and (h): $\alpha_{\rm 0.9\ cm-1.3\ mm}$ ranges from 2.47–2.94, being lower to the east. MM2 is undetected ($<4\sigma$) in the 3 cm VLA image. To estimate the 3 cm upper limits for MM2E and MM2W, we measure the peak intensity of the 3 cm emission within the 10% contour of the 0.9 cm emission, yielding $<$19.1 μJy beam^{-1} ($\sim 3.4\sigma$).

The $\alpha_{\rm 0.9\ cm-1.3\ mm}$ values and 3 cm nondetections of MM2E and MM2W indicate partially optically thick thermal dust emission. Extrapolating the S_ν of MM2E and MM2W from the 1.3 mm $R = -1.0$ image (Table 2) to 3 cm using the shallowest

Table 1
Observational and Image Parameters

	ALMA				VLA	
Parameter	Cycle 6	Cycle 4	Cycle 2	Cycles 3–5		
Wavelength	1.3 mm	1.3 mm	1.05 mm	0.82 mm	3 cm	0.9 cm
Observing date(s) (UT)	2019 Jul 15–16	2017 Aug 7–9	2015 May 14	2018 Jul 10, Aug 16 2017 Apr 22, 26 2016 Apr 9	2015 Jun 25	2015 Feb 9–10
Project code(s)	2018.1.01010.S	2016.1.01147.S	2013.1.00812.S	2015.1.00827.S, 2017.1.01373.S	15A-232	15A-232
Configuration(s)	C43-8	C40-7	C34-3(4)	C43-1, C43-2, C40-3, C36-2/3	A	B
Number(s) of antennas	42	45	37	41-46	27	26-27
Phase Center (J2000):						
R.A.	$18^h13^m58\overset{s}{.}1099$	$18^h13^m58\overset{s}{.}1099$	$18^h13^m58\overset{s}{.}110$[a]	$18^h13^m57\overset{s}{.}8599$	$18^h13^m58\overset{s}{.}10$	$18^h13^m58\overset{s}{.}10$
decl.	$-18°54'20\overset{''}{.}141$	$-18°54'20\overset{''}{.}141$	$-18°54'22\overset{''}{.}141$[a]	$-18°54'13\overset{''}{.}958$	$-18°54'16\overset{''}{.}7$	$-18°54'16\overset{''}{.}7$
Primary beam (FWHP)	$26''$	$26''$	mosaic	$17''$	$4'$	$1\overset{'}{.}3$
Frequency coverage[b]:						
Lower band (LSB)	220.530 GHz	220.530 GHz	278.23 GHz	358.02 GHz	9 GHz	31 GHz
center(s)	221.500 GHz	221.500 GHz				
Upper band (USB)	235.780 GHz	235.780 GHz	290.62 GHz		11 GHz	35 GHz
center(s)	238.850 GHz	238.850 GHz	292.03 GHz			
Bandwidth(s)[b]	4 × 937.5 MHz	1 × 468.75 MHz 3 × 937.5 MHz	2 × 1.875 GHz 117.2 MHz	1.875 GHz	2 × 2.048 GHz	4 × 2.048 GHz
Channel spacing(s)[b]	0.244 MHz	0.122 MHz 0.244 MHz 0.488 MHz	0.977 MHz 0.122 MHz	0.977 MHz	1 kHz	1 kHz
Gain calibrator(s)	J1832–2039	J1832–2039	J1733–1304	J1911–2006, J1733–1304	J1832–2039	J1832-2039
Bandpass calibrator	J1924–2914	J1924–2914	J1733–1304	J1924–2914	J1924–2914	J1924–2914
Flux calibrator(s)	J1924–2914	J1733–1304	Titan	J1924–2914, Titan	J1331+3030	J1331+3030
Projected baselines (kλ)	84–6298	14–2787	20–528	14–583	17–1221	9–1225
Largest angular scale (LAS)[c]	$0\overset{''}{.}8$	$1\overset{''}{.}4$	$4\overset{''}{.}2$	$4\overset{''}{.}5$	$3\overset{''}{.}4$	$4\overset{''}{.}2$
Reference(s)[d]	…	I18	C17	…	I16,C17	I16,C17
Robust parameter (R)	various (as indicated below)		0.5	0.5	0.5	0.0
Synthesized beam[e] (mas × mas[PA])	$R = +1$: 104 × 81 [−82°] $R = 0$: 57 × 41 [+64°] $R = -1$: 40 × 32 [+68°]		534 × 387 [−83°]	574 × 433 [−80°]	298 × 168 [0°]	270 × 144 [−6°]
rms noise[f] (mJy beam^{-1}):						
Continuum	$R = +1$: 0.034 $R = 0$: 0.038 $R = -1$: 0.074		…	…	0.0056	0.0084
Spectral line	$R = 0.5$: 0.68 $R = 0$ (^{13}CO): 0.91		4.9 ($\Delta v = 1.0$ km s^{-1}) 2.8-3.5 ($\Delta v = 1.2$ km s^{-1})	1.2	…	…

Notes.
[a] Central pointing.
[b] ALMA 1.05 and 0.82 mm: details only for spw(s) containing lines discussed in this Letter. The narrow 1.05 mm spw targeted H_2CO $4_{0,4}-3_{0,3}$ at 290.62341 GHz. Band centers: ALMA: rest frequency, VLA: sky frequency.
[c] Estimated using the analysisUtils task `au.estimateMRS` from the fifth percentile shortest baseline.
[d] Data previously published in I18: Ilee et al. (2018), C17: Cyganowski et al. (2017), I16: Ilee et al. (2016).
[e] For the continuum image, except for ALMA 1.05 and 0.82 mm, where it is for the line shown in Figure 3. *u,v* ranges were used for the 1.3 mm (>25 kλ) and 3 cm (>1300m ≈ 43 kλ) continuum images due to sparse sampling of shorter spacings and to minimize artifacts from the G11.94−0.62 H II region, respectively.
[f] Measured near MM2. Median values are quoted for line data (Δv is the channel width); the rms varies channel to channel due to variations in atmospheric opacity and bright and/or poorly imaged extended structures within the field of view (see also Cyganowski et al. 2017).

observed $\alpha_{0.9\,\mathrm{cm}-1.3\,\mathrm{mm}} = 2.47$ predicts $S_{3\,\mathrm{cm}} = 8 \pm 1$ and 4.7 ± 0.9 μJy, respectively, consistent with our 3 cm nondetections. As an additional check, we fit the 0.9 cm image with two 2D Gaussian components, fixing their positions to those of MM2E and MM2W from Section 3.1 and noting that in the lower-resolution 0.9 cm image, the western component represents a combination of the compact source MM2W and diffuse emission. Extrapolating these fitted 0.9 cm flux densities (Table 2) predicts $S_{3\,\mathrm{cm}} = 8 \pm 4$ and 11 ± 8 μJy, again consistent with our 3 cm nondetections.

3.3. Line Absorption from the Compact Core

To identify molecular gas potentially associated with the compact millimeter continuum sources, we searched for $\geqslant 4\sigma$ emission or absorption that spanned $\geqslant 2$ adjacent channels in

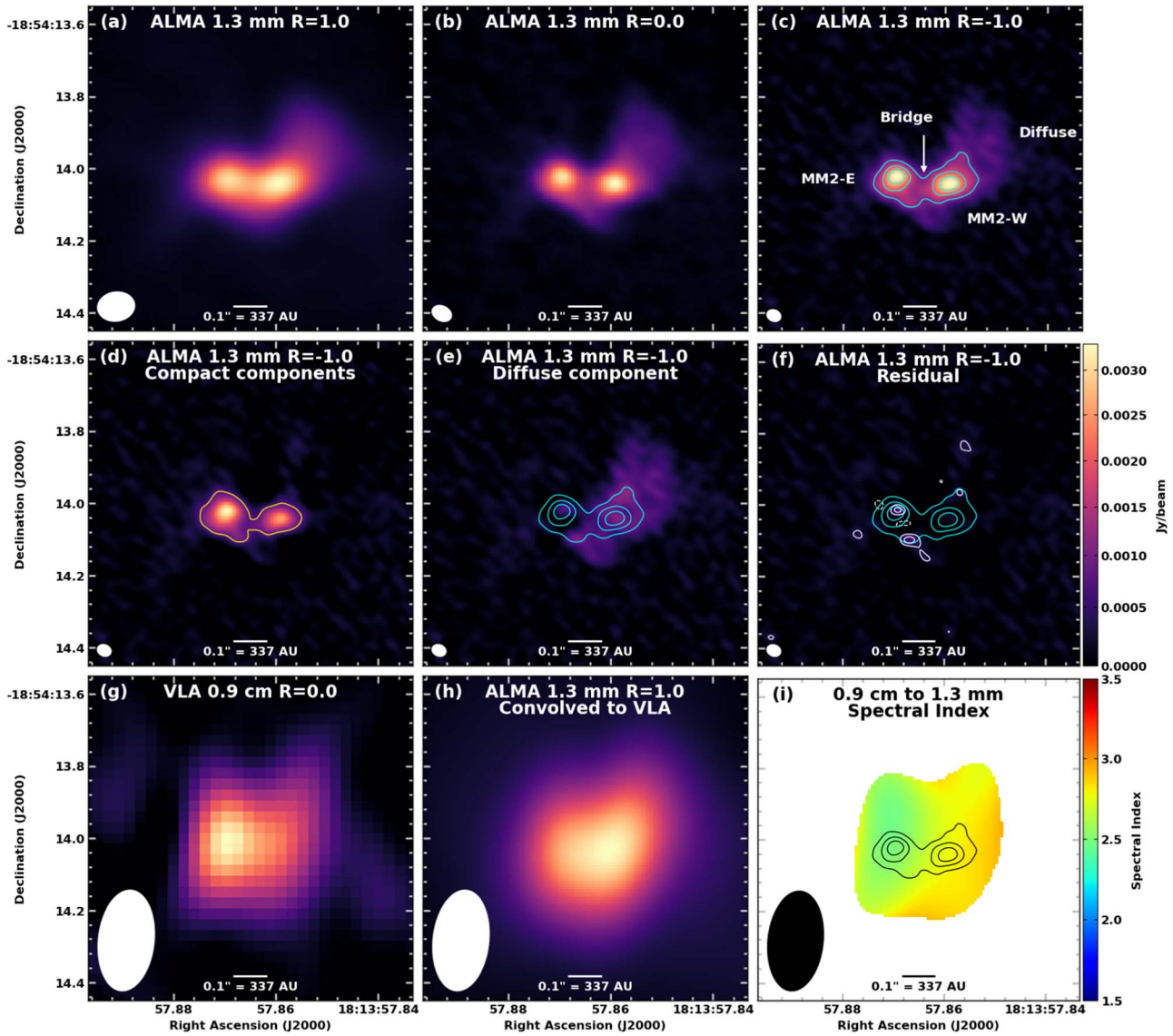

Figure 1. (a)–(c): ALMA 1.3 mm continuum images made with robust parameters of (a) $R = 1.0$, (b) $R = 0.0$, and (c) $R = -1.0$, with millimeter sources labeled in (c). (d)–(f): $R = -1.0$ images of (d) the two compact components only, (e) the diffuse component only, and (f) the residual of the simultaneous three-component fit (Section 3.1). (d) and (f) also show contours of the image shown in color scale, levels: (d) [10] $\times \sigma$ (yellow), (f) [4,7] $\times \sigma$ (solid white), [−4] $\times \sigma$ (dashed white), $\sigma = 7.4e-5$ Jy beam^{-1}. (g)–(h): ALMA 1.3 mm (g) and VLA 0.9 cm (h) images convolved to a common beam ($0\farcs280 \times 0\farcs155$, PA $= -6\fdg2$). (i): spectral index image created from (g) and (h), masked at the 5σ level. Panels (d)–(f) are displayed using a common color scale, shown to the right of (f); panels (a)–(c) and (g)–(h) similarly use a power-law stretch with exponent = 0.9 and a minimum of 0.0, but with the maximum set to the peak value for MM2 of each individual image. Contours of the $R = -1.0$ Planck T_b image are overplotted in cyan in (c) and (e)–(f) and in black in (i), levels: [25, 40, 55 K]. The synthesized beam is shown at the lower left in each panel.

the combined 1.3 mm line cubes at the positions of MM2E and MM2W (Table 2). The only line detected in these high-resolution data (beam $\lesssim 0\farcs08 \approx 270$ au) is ^{13}CO $J = 2$–1 ($\nu_{\rm rest} = 220.398684$ GHz, $E_{\rm upper} = 16$ K), in absorption against the 1.3 mm continuum.

To study the ^{13}CO absorption, we imaged this line with $R = 0$, a compromise between spatial resolution and signal-to-noise ratio (S/N) that yields a synthesized beam size of $0\farcs069 \times 0\farcs050$ ($\approx 230 \times 170$ au). Figure 2(a), a map of the minimum value of the ^{13}CO spectrum at each pixel, illustrates the spatial morphology of the absorption. Notably, absorption extends across MM2E, MM2W, and the continuum "bridge" but the depth of the absorption does not exactly follow the strength of the 1.3 mm continuum. The deepest absorption toward MM2E is $0\farcs006$ (20 au) east of the strongest continuum emission, while toward MM2W the deepest absorption is $0\farcs008$ (27 au) northwest of the continuum peak. Gaussian fitting of the absorption profiles (Figures 2(b)–(d)) yields similar centroid velocities for MM2E and MM2W, while MM2W has a broader line width ($\Delta v_{\rm FWHM} = 4.6 \pm 0.4$ and 6.5 ± 0.6 km s^{-1}, respectively). Taken together, these results suggest the ^{13}CO absorption traces gas physically associated with MM2E and MM2W, rather than e.g., a line-of-sight foreground cloud. This is reminiscent of the scenario outlined in Sahu et al. (2019) where an absorbing layer of cooler molecular material surrounds the optically thick protostar and binary member NGC 1333–IRAS4A1, which exhibits a millimeter dust T_b (∼60 K) similar to MM2E and MM2W.

3.4. Outflow Line Emission

Molecular outflows are clear signposts of protostars that have revealed star formation activity in other candidate

Table 2
Fitted Source Properties

Source	Position (J2000)[a]		Peak Intensity[a]	Integ. flux[a]	T_b[b]	Size[a]	Size[a]
	α (^{h} ^{m} ^{s})	δ ($^\circ$ $'$ $''$)	(mJy beam^{-1})	Density (mJy)	(K)	($''\times''$ [P.A.($^\circ$)])	(au × au)
ALMA 1.3 mm $R = -1.0$							
MM2E	18:13:57.86993	−18:54:14.0305	2.91 (0.07)	17.9 (0.5)	68.4	0.085 × 0.078 (0.003) [+55 (21)]	286 × 262 (9)
MM2W	18:13:57.85941	−18:54:14.0445	2.42 (0.07)	10.8 (0.4)	64.6	0.088 × 0.048 (0.004) [+111 (3)]	295 × 163 (12)
Diffuse	18:13:57.8570	−18:54:14.006	0.94 (0.03)	39 (1)	22.7	0.305 × 0.169 (0.01) [+135 (2)]	1029 × 570 (35)
VLA 0.9 cm $R = 0.0$[c]							
MM2E	fixed	fixed	0.139 (0.008)	0.14 (0.02)	4.9	<0.270 × <0.144	<910 × <485
MM2W+diffuse	fixed	fixed	0.094 (0.009)	0.21 (0.03)	6.3	0.213×0.197 (0.09) [+83 (61)]	718 × 664 (300)

Notes.
[a] Properties from 2D Gaussian fitting (Section 3.1): "size" is the FWHM deconvolved source size, statistical uncertainties are given in parentheses or indicated by the number of significant figures.
[b] Planck T_b calculated from S_ν and FWHM fitted size.
[c] Positions fixed to those of MM2E/MM2W from the 1.3 mm fit. For MM2E, the beam size is used in calculating T_b and reported as an upper limit for the size, as the source could not be deconvolved from the beam.

high-mass starless cores (e.g., Duarte-Cabral et al. 2013; Tan et al. 2016; Pillai et al. 2019). While ^{13}CO is not detected in emission near MM2 in our high-resolution data, low-excitation lines of CH_3OH and H_2CO provide alternative tracers of outflows from low- and high-mass protostars (Brogan et al. 2009; Morii et al. 2021; Tychoniec et al. 2021). Fortuitously, the tuning and larger largest angular scale of our deep 0.82 mm ALMA observations (Table 1) provide an opportunity to search for outflow activity from MM2E/MM2W using CH_3OH $4_{-1,3}$–$3_{0,3}$ ($\nu_{\rm rest} = 358.605799$ GHz, $E_{\rm upper} = 44$ K). Figure 3 shows channel maps of this CH_3OH line, illustrating that on the larger scales probed by these data (beam $0\farcs50 \approx 1685$ au), MM2 lies on a filament aligned roughly N–S (see also Cyganowski et al. 2017). At the positions of MM2E and MM2W, the CH_3OH emission from the filament peaks at ∼37 km s^{-1}. Taking this estimate of MM2's systemic velocity, blueshifted CH_3OH emission extends southwest of MM2E/MM2W, while redshifted CH_3OH emission lies to the northeast (Figures 2(e) and 3). This kinematic morphology suggests an asymmetric bipolar molecular outflow driven by MM2E and/or MM2W. The projected length and velocity extent are ∼12,600 au and 13 km s^{-1} for the blueshifted lobe and ∼5,100 au and 2 km s^{-1} for the redshifted lobe (lengths are the average of estimates assuming the driving source is MM2E/MM2W). These values imply dynamical timescales of $t_{\rm dyn} \sim 4600$ yr and ∼12,100 yr for the blue and red lobes. We emphasize, however, that the CH_3OH emission is unlikely to trace the highest-velocity gas (see the ^{12}CO/H_2CO comparison for a low-mass outflow in Cyganowski et al. 2017) so these $t_{\rm dyn}$ estimates should be interpreted with caution.

To check for evidence of this outflow in other lines, we re-imaged the five H_2CO and CH_3OH transitions with $E_{\rm upper} <$ 100 K in the 1.05 mm tuning of Cyganowski et al. (2017). Figure 3 shows H_2CO $4_{0,4}$–$3_{0,3}$ ($\nu_{\rm rest} = 290.62341$ GHz, $E_{\rm upper} = 35$ K), the closest to CH_3OH $4_{-1,3}$–$3_{0,3}$ in $E_{\rm upper}$ and line strength, and the only 1.05 mm line observed with sufficient spectral resolution to image with $\Delta v = 1$ km s^{-1} (Table 1; the others were imaged with $\Delta v = 1.2$ km s^{-1}). The behavior of this H_2CO line is representative of the 1.05 mm H_2CO and CH_3OH transitions, with similar morphology to CH_3OH $4_{-1,3}$–$3_{0,3}$ in channels near the systemic velocity (Figure 3), but outflow emission detected over a narrower velocity range and at lower S/N due to the lower sensitivity of the data (Table 1). Figure 2(f) summarizes the proposed morphology of the core/outflow system.

4. Discussion

To explore the nature of MM2E and MM2W, we first consider their observed 1.3 mm continuum brightness temperatures (T_b), which provide strict lower limits for their physical temperatures of 68.4 K and 64.6 K, respectively (Table 2). These high temperatures signify internal heating, as external heating (by MM1 and the intermediate- or high-mass protostar MM3; Cyganowski et al. 2009, 2011, 2017) could account for dust temperatures of at most ∼23 K, based on simple estimates (see also Cyganowski et al. 2014). With evidence for both internal heating and a bipolar outflow (Section 3.4), we interpret MM2E and MM2W as deeply embedded protostars, which leads to the conclusion that MM2 is not starless and emphasizes the importance of high-resolution (sub)millimeter observations for detecting protostars and their outflows in candidate high-mass starless clumps and cores (see also, e.g., Duarte-Cabral et al. 2013; Tan et al. 2016; Pillai et al. 2019; Svoboda et al. 2019).

Observed (sub)millimeter T_b can be used to estimate the total luminosities (L_*) of deeply embedded protostars in the context of a simple model of blackbody emission from an optically thick dust shell surrounding them (e.g., Brogan et al. 2016; Ginsburg et al. 2017; Hunter et al. 2017), via $L_* = 4\pi r^2 \sigma T_b^4$, where r is the radius of the $\tau \approx 1$ sphere and σ is the Stefan–Boltzmann constant. Because the observed dust emission is not entirely optically thick toward MM2E and MM2W (Section 3.2, Figure 1(i)), the observed T_b will underestimate the dust temperature and L_* will be a lower limit. Using their fitted sizes and Planck T_b (calculated from the integrated flux densities and fitted sizes; Table 2), we estimate $L_* > 24.7\ L_\odot$ for MM2E and $L_* > 12.6\ L_\odot$ for MM2W. Notably, these limiting values are one to four orders of magnitude higher than those estimated for the low-mass members of the NGC 6334I protocluster using the same approach (MM5-9, Table 5 of Brogan et al. 2016). Although our limiting luminosities for MM2E/MM2W are ∼3 orders of magnitude lower than those estimated with this method for W51e2e and for NGC 6334I–MM1in outburst ($2.3 \times 10^4\ L_\odot$ and $4.2 \times 10^4\ L_\odot$, respectively; Ginsburg et al. 2017; Hunter et al. 2017), massive protostars

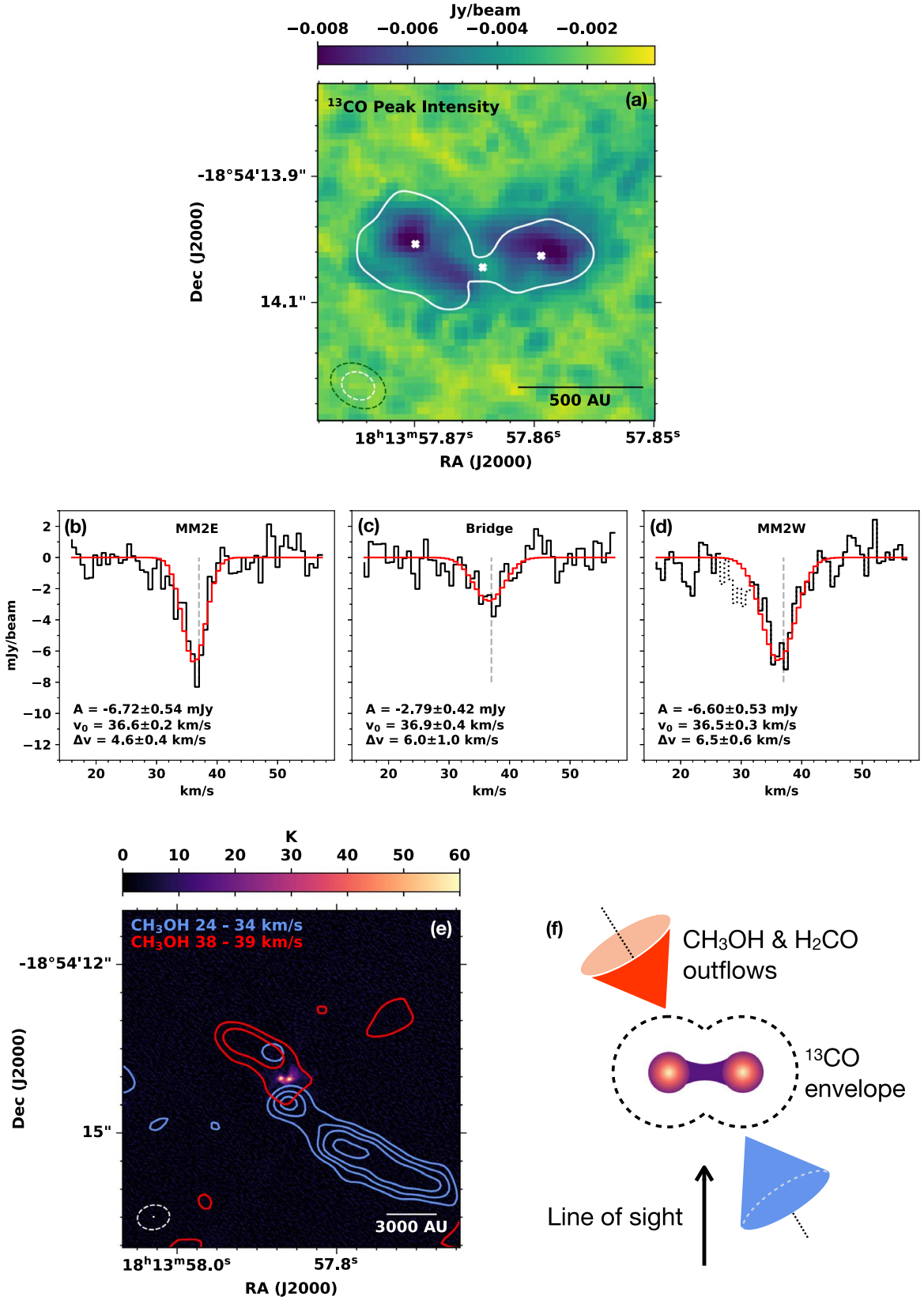

Figure 2. (a): Zoom of MM2 showing the minimum map of the ^{13}CO $J = 2$–1 absorption. The white 10σ continuum contour from Figure 1(d) shows the "bridge" (Section 3.1). Crosses mark pixels for which spectra are shown. (b)–(d): ^{13}CO $J = 2$–1 spectra (black) at the fitted continuum positions of MM2E and MM2W and a "bridge" pixel, overplotted with Gaussian fits to the line core (red; the MM2W fit excludes the channels shown with a dotted line). The estimated systemic velocity (37 km s^{-1}, Section 3.4) is shown as a dashed gray line; labels give best-fit parameters. (e): 1.3 mm Planck T_b ($R = -1$) image overlaid with contours of integrated red/blueshifted CH_3OH $4_{-1,3}$–$3_{0,3}$ emission. Levels: [4,7] $\times\ \sigma = 3.3$ mJy beam^{-1} km s^{-1} (red), [4, 7, 10, 15] $\times\ \sigma = 5.5$ mJy beam^{-1} km s^{-1} (blue). (f): Proposed morphology of MM2, viewed perpendicular to the line of sight. (a) and (e): ALMA synthesized beams are shown at the bottom left.

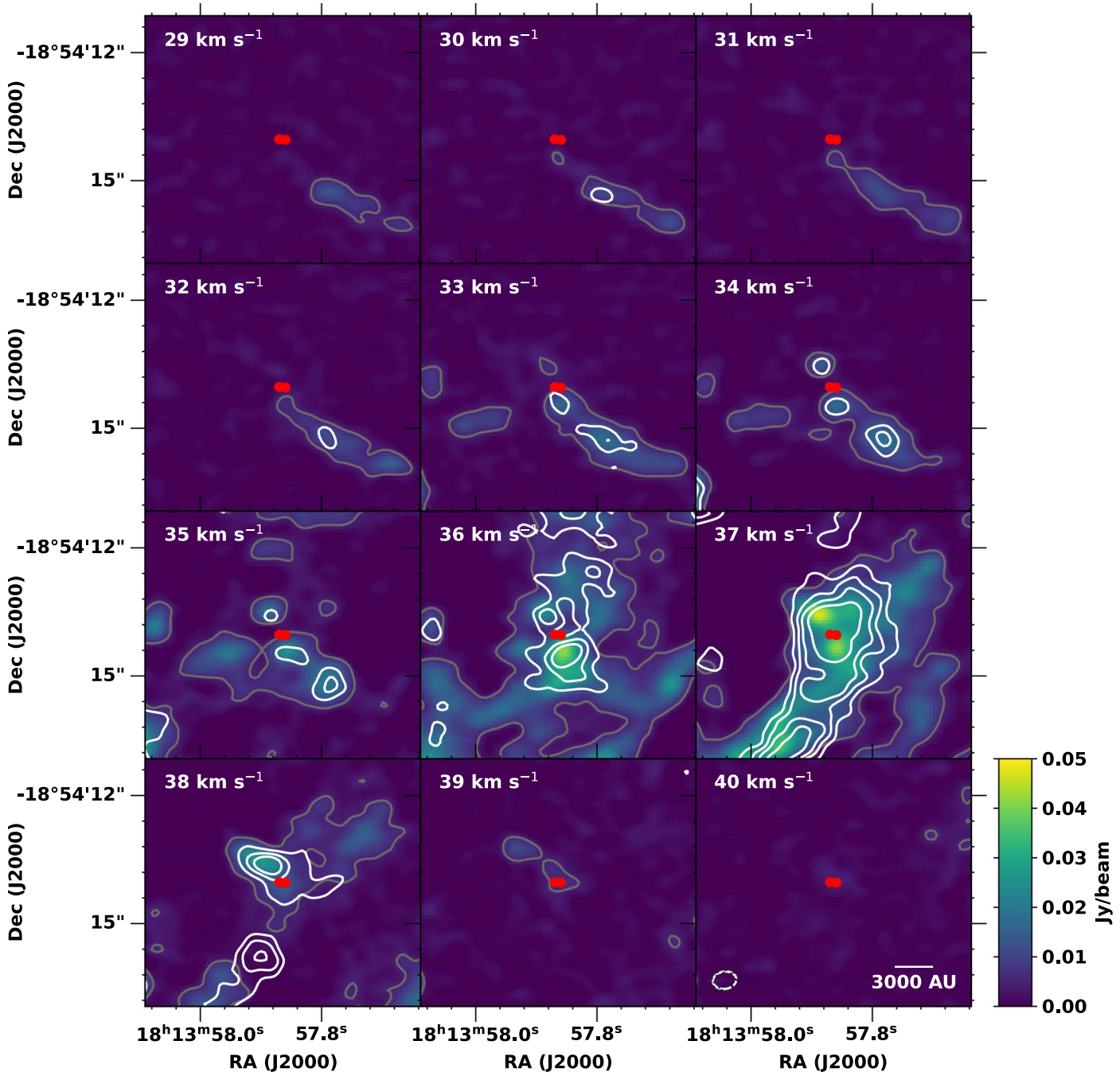

Figure 3. Channel maps showing CH_3OH $4_{-1,3}$–$3_{0,3}$ (color scale and gray contour, $4 \times \sigma = 1.2$ mJy beam^{-1}) and H_2CO $4_{0,4}$–$3_{0,3}$ (white contours, [4,7,10,15] $\times \sigma = 4.9$ mJy beam^{-1}) emission. Red circles mark the positions of MM2E and MM2W (Table 2).

are expected to pass through a low-luminosity stage early in their evolution (e.g., Kuiper & Yorke 2013).

The closest analog to MM2E and MM2W in the literature is NGC 6334I–MM4A, an optically thick dust source, in a massive protocluster, that lacks compact thermal molecular line emission in ALMA observations despite a high dust T_b (97 ± 5 K; Brogan et al. 2016). NGC 6334I–MM4A drives a collimated bipolar outflow detected in dense gas tracers and exhibits faint, variable water maser emission (Brogan et al. 2018). Although previous surveys found no water masers toward MM2 (Hofner & Churchwell 1996; Breen & Ellingsen 2011), masers with luminosity similar to those in NGC 6334I–MM4A would be only ∼0.05 Jy at G11.92−0.61's distance and would have been undetected by these surveys, particularly at velocities where the bright MM1 maser limits the image dynamic range. An analog in a low-mass multiple system is component B of IRAS 16293–2422, a partially optically thick dust source with $T_{b,\mathrm{mm}} \sim 180$ K, interpreted as a very young protostar (Chandler et al. 2005; Hernández-Gómez et al. 2019). To our knowledge, MM2E/MM2W is the first example of a system of two nearly optically thick millimeter dust sources.

Comparing our results with model predictions (Section 1), the observed properties of MM2E and MM2W in many respects match the super-Alfvénic cases of Mignon-Risse et al. (2021)remarkably well, suggesting that this protobinary may be forming in an environment with a weak magnetic field. MM2E

and MM2W have similar 1.3 mm T_b and S_ν (ratio E:W = 1.06 and 1.66, respectively), suggesting that the mass ratio of the two protostars is likely comparable to the ≈1.1–1.6 range of the Mignon-Risse et al. (2021) simulations. The observed separation of MM2E and MM2W (∼505 au) is similarly consistent with the Mignon-Risse et al. (2021) results (binary separations 350–700 au), and the "bridge" we observe is qualitatively similar to linking structures visible in the simulated column density maps in their Figure 8. Interestingly, linking "bridges" form in simulations of binary formation via both core (e.g., Riaz et al. 2014; for ∼equal-mass low-mass binaries) and disk fragmentation (e.g., Mignon-Risse et al. 2021, in which disk fragmentation is precipitated by the collision of extended spiral arms).

In the Mignon-Risse et al. (2021) simulations, the individual protostars have Keplerian disks with diameters of ∼200–400 au, which are embedded within a transient disk-like circumbinary structure. With no detected line emission in our high-resolution observations, it is unclear whether MM2E and MM2W exhibit Keplerian rotation. Their fitted sizes (Table 2) are, however, comparable to the simulation's individual disk diameters, with the more extended millimeter emission potentially tracing a circumbinary disk. The total circumprotostellar gas mass from the sum of the fitted VLA 0.9 cm flux densities is $6.8 \pm 0.9\ M_\odot$ (considering the fitting uncertainties from Table 2, added in quadrature, and 10% calibration uncertainty) using $T_{\rm dust} = 66.5$ K (the average 1.3 mm T_b for MM2E/MM2W) and, followingthe approach of Karnath et al. (2020), assuming the 0.9 cm emission is optically thin, a gas:dust mass ratio of 100:1, and $\kappa_{0.9\ \rm cm} = 0.128\ \rm cm^2\ g^{-1}$.

Notably, this estimate is comparable to the sum of the virial masses calculated from the ^{13}CO line widths (Section 3.3): Assuming spherical clouds with $1/r$ density profiles (Carpenter et al. 1990), angular diameters equal to the geometric means of the 1.3 mm fitted sizes (Table 2), and correcting for a mean inclination of the rotation axis to the line of sight (30°) yields $3.5 \pm 0.8\ M_\odot$ for MM2E and $5.7 \pm 1.0\ M_\odot$ for MM2W for a total of $9.2 \pm 1.2\ M_\odot$. To test the dependence on the assumed angular diameter, we used a similar fitting procedure to obtain source sizes from the $R = 0$ 1.3 mm continuum image, which yields a combined virial mass of $9.0 \pm 1.2\ M_\odot$. The combined virial mass of $\approx 9 \pm 1\ M_\odot$ minus the gas mass estimate allows for central protostars of current mass $\sim 1\ M_\odot$. Depending on their evolutionary track, the L_* (including accretion) of such protostars can reach values of $\sim 25\ L_\odot$ (Young & Evans 2005) to $> 10^3\ L_\odot$ (Kuiper & Yorke 2013), consistent with the L_* lower limits that we derive from the dust T_b of MM2E and MM2W. Considering the luminosity limits, protostellar mass estimates and dust properties derived above together with theoretical expectations, we interpret MM2E and MM2W as a young proto-high-mass-binary system.

The outflow from MM2E/MM2W (Section 3.4, Figures 2(e) and 3) provides evidence for ongoing accretion onto the growing protobinary system. With ample fuel available within the gas-rich protocluster environment, the protostellar masses (and luminosities) are expected to increase with time. Accretion will also affect the binary separation, which can increase or decrease depending on turbulence, magnetic field strength, and the presence of outflows, with magnetic fields promoting the formation of close high-mass binary systems (e.g., Lund & Bonnell 2018; Harada et al. 2021; Ramírez-Tannus et al. 2021). Future high-resolution observations of MM2E/MM2W—at shorter wavelengths to better measure the protostellar luminosities, at longer wavelengths to search for line emission in a regime where the dust is optically thin, and in full polarization to measure the magnetic field—will provide a powerful test case for models of high-mass binary formation.

The National Radio Astronomy Observatory is a facility of the National Science Foundation operated under cooperative agreement by Associated Universities, Inc. This paper makes use of the following ALMA data: ADS/JAO.ALMA#2013.1.00812.S, ADS/JAO.ALMA#2015.1.00827.S, ADS/JAO.ALMA#2016.1.01147.S, ADS/JAO.ALMA#2017.1.01373.S, and ADS/JAO.ALMA#2018.1.01010.S. ALMA is a partnership of ESO (representing its member states), NSF (USA) and NINS (Japan), together with NRC (Canada), MOST and ASIAA (Taiwan), and KASI (Republic of Korea), in cooperation with the Republic of Chile. The Joint ALMA Observatory is operated by ESO, AUI/NRAO and NAOJ. C.J.C. acknowledges support from the University of St Andrews Restarting Research Funding Scheme (SARRF), which is funded through the SFC grant reference SFC/AN/08/020. J.D.I. acknowledges support from the UK's STFC under ST/T000287/1. S.Z. is funded by the China Scholarship Council–University of St Andrews Scholarship (PhD programmes, No. 201806190010). T.J. Haworth is funded by a Royal Society Dorothy Hodgkin Fellowship. This research made use of NASA's Astrophysics Data System Bibliographic Services and APLpy, an open-source plotting package for Python (Robitaille & Bressert 2012).

ORCID iDs

C. J. Cyganowski https://orcid.org/0000-0001-6725-1734
J. D. Ilee https://orcid.org/0000-0003-1008-1142
C. L. Brogan https://orcid.org/0000-0002-6558-7653
T. R. Hunter https://orcid.org/0000-0001-6492-0090
S. Zhang (张遂楠) https://orcid.org/0000-0002-8389-6695
T. J. Harries https://orcid.org/0000-0001-8228-9503
T. J. Haworth https://orcid.org/0000-0002-9593-7618

References

Beltrán, M. T., Cesaroni, R., Moscadelli, L., et al. 2016, A&A, 593, A49
Beuther, H., Linz, H., Henning, T., Feng, S., & Teague, R. 2017, A&A, 605, A61
Breen, S. L., & Ellingsen, S. P. 2011, MNRAS, 416, 178
Brogan, C. L., Hunter, T. R., Cyganowski, C. J., et al. 2009, ApJ, 707, 1
Brogan, C. L., Hunter, T. R., Cyganowski, C. J., et al. 2016, ApJ, 832, 187
Brogan, C. L., Hunter, T. R., Cyganowski, C. J., et al. 2018, ApJ, 866, 87
Carpenter, J. M., Snell, R. L., & Schloerb, F. P. 1990, ApJ, 362, 147
Chandler, C. J., Brogan, C. L., Shirley, Y. L., & Loinard, L. 2005, ApJ, 632, 371
Chini, R., Hoffmeister, V. H., Nasseri, A., Stahl, O., & Zinnecker, H. 2012, MNRAS, 424, 1925
Cyganowski, C. J., Brogan, C. L., Hunter, T. R., et al. 2012, ApJL, 760, L20
Cyganowski, C. J., Brogan, C. L., Hunter, T. R., et al. 2014, ApJL, 796, L2
Cyganowski, C. J., Brogan, C. L., Hunter, T. R., et al. 2017, MNRAS, 468, 3694
Cyganowski, C. J., Brogan, C. L., Hunter, T. R., & Churchwell, E. 2009, ApJ, 702, 1615
Cyganowski, C. J., Brogan, C. L., Hunter, T. R., Churchwell, E., & Zhang, Q. 2011, ApJ, 729, 124
Duarte-Cabral, A., Bontemps, S., Motte, F., et al. 2013, A&A, 558, A125
Ginsburg, A., Goddi, C., Kruijssen, J. M. D., et al. 2017, ApJ, 842, 92
Gravity Collaboration, Karl, M., Pfuhl, O., et al. 2018, A&A, 620, A116

Harada, N., Hirano, S., Machida, M. N., & Hosokawa, T. 2021, MNRAS, 508, 3730
Hernández-Gómez, A., Loinard, L., Chandler, C. J., et al. 2019, ApJ, 875, 94
Hofner, P., & Churchwell, E. 1996, A&AS, 120, 283
Hunter, T. R., Brogan, C. L., Cyganowski, C. J., & Schnee, S. 2015, Conditions and Impact of Star Formation, Vol. 75–76 (Les Ulis: EDP Sciences), 285
Hunter, T. R., Brogan, C. L., MacLeod, G., et al. 2017, ApJL, 837, L29
Ilee, J. D., Cyganowski, C. J., Brogan, C. L., et al. 2018, ApJL, 869, L24
Ilee, J. D., Cyganowski, C. J., Nazari, P., et al. 2016, MNRAS, 462, 4386
Karnath, N., Megeath, S. T., Tobin, J. J., et al. 2020, ApJ, 890, 129
Koumpia, E., de Wit, W. J., Oudmaijer, R. D., et al. 2021, A&A, 654, A109
Kraus, S., Kluska, J., Kreplin, A., et al. 2017, ApJL, 835, L5
Krumholz, M. R., Klein, R. I., McKee, C. F., Offner, S. S. R., & Cunningham, A. J. 2009, Sci, 323, 754
Kuiper, R., & Yorke, H. W. 2013, ApJ, 772, 61
Lund, K., & Bonnell, I. A. 2018, MNRAS, 479, 2235
Meyer, D. M. A., Kuiper, R., Kley, W., Johnston, K. G., & Vorobyov, E. 2018, MNRAS, 473, 3615
Mignon-Risse, R., González, M., Commerçon, B., & Rosdahl, J. 2021, A&A, 652, A69
Morii, K., Sanhueza, P., Nakamura, F., et al. 2021, ApJ, 923, 147
Oliva, G. A., & Kuiper, R. 2020, A&A, 644, A41
Pillai, T., Kauffmann, J., Zhang, Q., et al. 2019, A&A, 622, A54
Pomohaci, R., Oudmaijer, R. D., & Goodwin, S. P. 2019, MNRAS, 484, 226
Ramírez-Tannus, M. C., Backs, F., de Koter, A., et al. 2021, A&A, 645, L10
Redaelli, E., Bovino, S., Giannetti, A., et al. 2021, A&A, 650, A202
Riaz, R., Farooqui, S. Z., & Vanaverbeke, S. 2014, MNRAS, 444, 1189
Robitaille, T., & Bressert, E. 2012, APLpy: Astronomical Plotting Library in Python, Astrophysics Source Code Library, ascl:1208.017
Rosen, A. L., & Krumholz, M. R. 2020, AJ, 160, 78
Rosen, A. L., Krumholz, M. R., McKee, C. F., & Klein, R. I. 2016, MNRAS, 463, 2553
Rosen, A. L., Li, P. S., Zhang, Q., & Burkhart, B. 2019, ApJ, 887, 108
Sahu, D., Liu, S.-Y., Su, Y.-N., et al. 2019, ApJ, 872, 196
Sana, H., Le Bouquin, J. B., Lacour, S., et al. 2014, ApJS, 215, 15
Sato, M., Wu, Y. W., Immer, K., et al. 2014, ApJ, 793, 72
Svoboda, B. E., Shirley, Y. L., Traficante, A., et al. 2019, ApJ, 886, 36
Tan, J. C., Kong, S., Zhang, Y., et al. 2016, ApJL, 821, L3
Tanaka, K. E. I., Zhang, Y., Hirota, T., et al. 2020, ApJL, 900, L2
Tychoniec, Ł., van Dishoeck, E. F., van't Hoff, M. L. R., et al. 2021, A&A, 655, A65
Young, C. H., & Evans, N. J. I. 2005, ApJ, 627, 293
Zapata, L. A., Garay, G., Palau, A., et al. 2019, ApJ, 872, 176
Zhang, Y., Tan, J. C., Tanaka, K. E. I., et al. 2019, NatAs, 3, 517